A versatile monolithic optoelectronic platform for bending angle sensing and visible light communication

Fan Shi (石帆)[1*], **Chengxiang Jiang (蒋呈祥)**[1], **Li Fang (房 力)**[1], **Zhihang Sun (孙志航)**[1], **Jiabin Yan (严嘉彬)**[1], **Hongbo Zhu (朱洪波)**[2], and **Yongjin Wang (王永进)**[1**]

[1] GaN Optoelectronic Integration International Cooperation Joint Laboratory of Jiangsu Province, Nanjing University of Posts and Telecommunications, Nanjing 210003, China

[2] Key Laboratory of Wireless Communications, Nanjing University of Posts and Telecommunications, Nanjing 210003, China

*Corresponding author: sf123@njupt.edu.cn
**Corresponding author: wangyj@njupt.edu.cn

In this letter, a kind of optoelectronic chip based on III-Nitride is developed as a versatile platform for both fiber-optic sensing and optical communication. The optoelectronic chip consists of a light-emitting diode (LED) and a photodiode (PD) which are fabricated with the same multi-quantum well (MQW) structure, and monolithically integrated on a sapphire substrate. By integrating the chip with a polydimethylsiloxane (PDMS) encapsulated silica fiber-optic sensor, it can effectively detect the bending-induced light intensity change, and generates the photocurrent to point out the angle changes. Besides, such optoelectronic chip can also be treated as a transceiver, enabling a duplex communication for real-time audio and video transmission. The proposed optoelectronic chip has the advantages of miniaturization, versatility and ease of massive manufacturing, making it promising in integrated optical sensing and communication (IOSAC) system.

Keywords: optoelectronic chip, fiber-optic sensing, LED.
DOI: xxxxxxx/COLxxxxxxx.

1. Introduction

With the emergence of Internet of Things (IoT), communication and interaction between objects become smart, efficient and convenient. Smart wearable devices possessing the ability of bending angle sensing and wireless communication play a key role in several IoT scenarios, including gesture recognition[1], remote healthcare[2], and human-machine interaction[3]. Optical sensors, especially fiber-optic sensors have the advantages of anti-corrosion, anti-electromagnetic interference, and light weight. These merits effectively circumvent the disadvantages of electrical sensors and ensure stable acquisition and transmission of signals. Intensity modulation and phase modulation are two typical techniques for optical sensors. Phase modulation techniques mainly rely on the construction of fiber-optic interference structures[6,7], which sense the changes by monitoring the wavelength shift. However, the assembly of broadband light source and spectrometer brings an expensive and complex system.

Intensity modulation techniques obtain the sensing information by directly monitoring the change of light intensity inside the fiber[8–10], resulting in a compact system, low-cost equipment and flexible configuration. For instance, Zhou et al[8]. presented a wide joint angle detection based on plastic optical fiber (POF), using a laser source and an optical power meter. Aitkulov et al[10]. investigated the breathing rate measurement based on a smartphone-integrated fiber bending sensor. Similarly, using flashlight and camera as light source and detector, different sensors are demonstrated, including temperature[11], humidity[12], and refractive index[13]. Although smartphones provide a versatile platform for intensity modulation based sensing, the flashlight and camera are solidified inside a phone and cannot be flexibly configured. In addition, high-speed optical communication links are hardly realized from the hardware inside a smartphone.

Nowadays, optoelectronic devices based on the III-nitride semiconductor material, especially GaN, has attracted interesting attentions in high-speed ultraviolet light communication[14,15], visible light communication (VLC)[16,17], luminescence enhancement[18,19], optical sensing[20,21] and display[22–24] due to its advantages in fast response time, stable crystal structure, and wide bandgap width. In particular, the coexistence of light emission and detection of GaN multiple quantum well

(MQW) makes it possible to construct a monolithic opto-electronic platform and promotes the rapid development of GaN-based optoelectronic sensors and on-chip communication. For example, Li et al[25]. present a monolithic integration of the LED, PD and waveguide on Si substrate and a 250 Mb/s on-chip communication has been demonstrated. Wang et al[26]. investigated a two-way optical link using a single transmitter and receiver based on GaN MQW III-nitride diodes. Luo et al[27]. report a chip-scale airflow sensor using a GaN-based optoelectronic device. Yu et al[28] demonstrated a dual-functional p-i-n diode capable of light emission and detection in the DUV band. Memon et al[29] report a dual-wavelength wireless optical communication by integrating a micro-LED array with quantum dots, achieving the data rate of 586 and 55 Mbps at the emission wavelengths of 275 and 470 nm.

　　In this work, a versatile optoelectronic platform with the monolithic integration of LED and PD has been developed to construct a fiber-optic bending angle sensing system and as well as visible duplex communication links. On the one hand, the millimeter-sized optoelectronic device highly integrates a light emitter and a receiver, which enables the construction of a miniaturized chip-integrated fiber bending sensing system. In this case, fiber deformation changes the light amount coupled from emitter to detector, introducing an angle-dependent photocurrent response. On the other hand, such optoelectronic device can be treated as a transceiver for duplex visible communication, and the corresponding uplink and downlink rates of 20 Mbps and 1 Mbps are obtained when pseudorandom binary sequence (PRBS) driven signals are applied.

2. Optoelectronic chip enabled fiber-optic bending sensing

2.1. The sketch diagram of the chip-integrated fiber sensing system

The sketch diagram of a chip-integrated angle-sensing system is shown in Fig. 1(a). Light emitted from an LED propagates along a leading-in fiber, passes through the sensing region, flows into a leading-out fiber, and is finally received by the on-chip PD. As force is applied over the sensitive region, butt-coupling angle between the leading-in and out fibers changes, which causes variation of the transmission optical power inside the leading-out fiber. Weak fluctuation of the optical power is then captured by the on-chip PD. Fig. 1(b) shows the microscope image of the chip under a biased voltage applied on the LED. It can be clearly seen that a bright light spot in the dark which denotes the light-emitting region. The butt-to-butt coupling of chip and optical fiber is carried out with the assistance of a fiber coupling platform, and the bird-view image is displayed in Fig. 1(c). Here the light emitting size is designed to be smaller than the diameter of the used fiber for a better butt coupling.
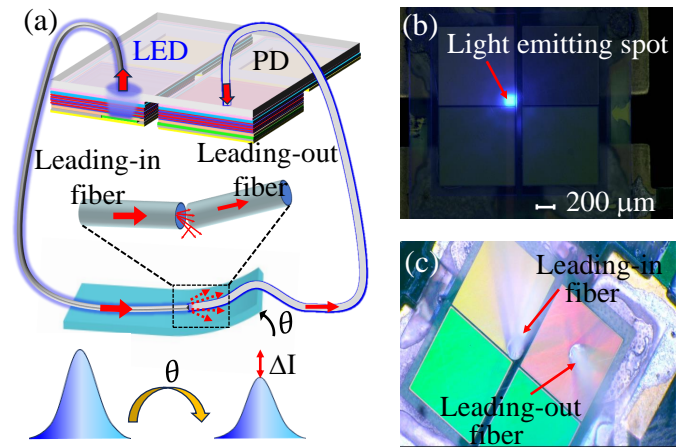

Fig. 1. (a) Schematic diagram of a chip-integrated fiber sensing system. (b) Optical images of the chip with a driven voltage applied to the LED. (c) Microscope image of the butt-coupling between optical fibers and chip.

2.2. Optoelectronic chip fabrication and Characterization

The optoelectronic chip is fabricated on a sapphire substrate based GaN wafer, as described in Fig. 2(a). The epitaxial structure is composed of undoped GaN, Si-doped GaN (n-GaN), MQW and Mg-doped GaN (p-GaN) from bottom to top. A 230-nm-thick transparent indium tin oxide (ITO) current spreading layer is deposited over p-GaN as a p-contact layer. Then two square regions with diameter of 0.1 mm and 1 mm are defined as the active areas for LED and PD units, respectively. Here, for micro-sized LED, inductively coupled plasma (ICP) is first used to etch the mesa with a footprint of 1×1 mm^2 and then the light emitting region of the micro-sized LED is defined through patterning the ITO layer with a size of 100 μm rather than ICP etching of GaN. A deep etching is employed to remove all epilayers between the LED and PD regions for device isolation. The metal stacks are further deposited on the n-GaN and ITO surfaces as the contact layer. After fabrication, the electrical and optical properties of the chip are characterized. As plotted in Fig. 2(b), current-voltage (I-V) curve is measured by using a semiconductor device analyzer (Agilent B1500A). The inset plots the capacitance–voltage (C-V) curve of the chip. An AC signal of 1 MHz with applied voltage is used in the C-V measurement. The capacitance is approximately 50 pF before the driven voltage reaches the turn-on voltage. Fig. 2(c) shows the emission and absorption spectra of LED and PD, respectively. As driven current increases, the light amount of LED significantly improves, and a larger overlapped region occurs. The light emission is an irreversible process to the light detection[30] that introduces a partially overlapped wavelength region, which is caused by the gravitational field[31]. The I-V characteristics of PD are measured under LED radiation with different driven currents, as presented in Fig. 2(d). Without LED radiation, the measured dark current is below 10^{-7} mA. When the PD is radiated by the LED, the photocurrent significantly rises and reaches to an order of 10^{-2} mA at a injection current of 10 mA. The light emission power of the LED at a driven current of 10
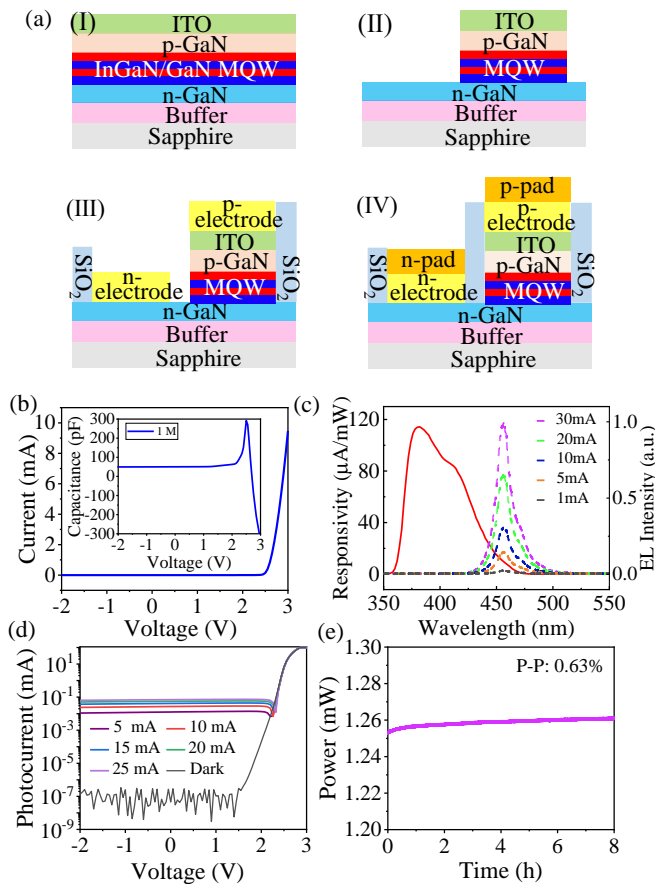
Fig. 2. (a) Schematic diagram of the chip fabrication process, including ITO deposition(I), Mesa definition and etching (II), electrodes deposition(III), and meta pads deposition(IV). (b) Current-voltage (I-V) curve of the LED, and the inset shows its C-V curve. (c) EL and RS spectra of the MQW-based structure. (d) Photocurrent response of the PD under LED radiation with different inject currents. (e) An 8-hour stability test of the LED light-emitting intensity .

mA is monitored over 8 h at room temperature, as recorded in Fig. 2(e). The peak-to-peak deviation is calculated to be 0.63%, which implies a good stability of the LED under a long-term operation.

2.3. Optical fiber sensor fabrication

To sense the bending angle, a fiber sensor consisting of two opposite aligned bare optical fibers (200 μm core diameter and NA=0.22) sealed in a PDMS patch is presented. Fabrication stages are illustrated in Fig. 3. The first step involves the pouring of the underlying PDMS film, which is then heated at 80° for 40 minutes to obtain a flat PDMS patch with 300 μm thickness. Afterwards the underlying PDMS patch is transferred and attached on the bottom of a deeper model with a 1 mm thickness groove. Next, a peice of optical fiber is attached straight to the underlying PDMS patch, scratched with a diamond blade at the middle, and covered by a stack of PDMS liquid on the top layer. After heating again, a 1 mm thick PDMS patch is formed with
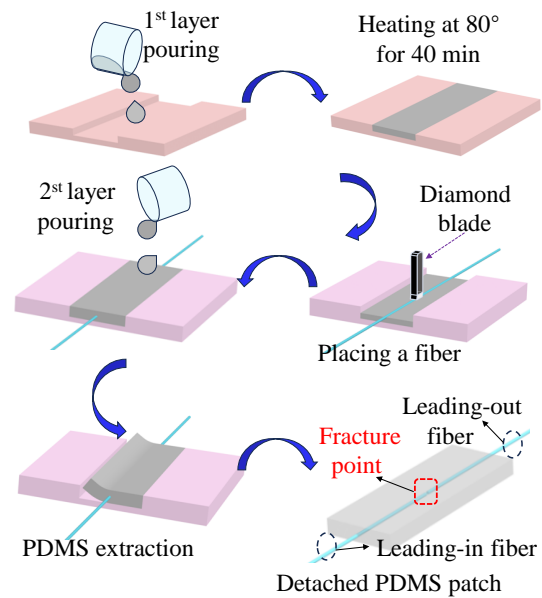

Fig. 3. Schematic diagram of the fabrication process of a PDMS-packaged fiber sensor.

the optical fiber firmly sealed in it. Finally, by slightly bending the middle part of the fiber, it is easily divided into two segments called the leading-in fiber and the leading-out fiber.

2.4. Experimental results for bending angle detection

The bending sensing performance is evaluated by measuring the photocurrent responses of the system under different bending angles. As force is applied on the sensitive region of the PDMS patch, the deformation of PDMS will bend the fiber inside, leading to a drop of the light coupling efficiency between the leading-in and leading-out fibers. In this case, the on-chip PD responses to the changed light intensity, and produces photocurrent to indicate the bending angles. As shown in Fig. 4(a), the photocurrent of PD decreases as the bending angle increases, and returns to the initial value (the pink baseline) once the bending is released. The measured photocurrent resembles a step-like trend, and a maximum photocurrent difference is about 410 nA when the bending angle changes from 0° to 40°. The symmetrical distribution of the steps indicates that the good reducibility of the PDMS encapsulated fiber sensor. As the bending angle exceeds 40 degrees, the photocurrent value changes slowly. This is because that the amount of light received in the leading-out fiber is low at large misalignment coupling angles, resulting in little change in photocurrent. The corresponding photocurrent values at different bending angles are recorded and plotted in Fig. 4(b). As can be seen from the data (black and red dots), the system has a relatively low hysteresis when applying and withdrawing bending, and the slope efficiency of the linear ranges from 10° to 30° is calculated to be -17.5 nA/°. Fig. 4(c) shows the dynamic photocurrent response of the PD under repetitive cycles of fiber bending and release. The photocurrent response can consistently reach and return
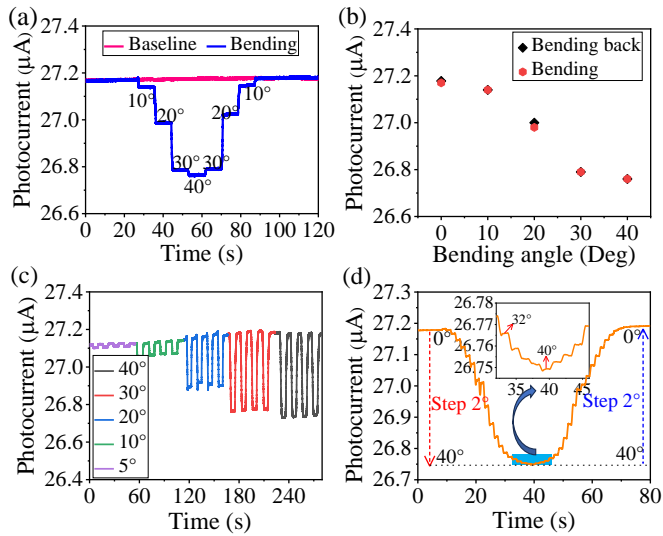
Fig. 4. Bending sensing performances of the chip-integrated fiber system. (a) The system baseline (pink line) and step-like photocurrent response (blue line) when bending angle continuously changes from 0° to 40°. (b) Extracted photocurrent values correspond to the bending angles. (c) Photocurrent response under instantaneous bending angle changes. (d) Photocurrent response of the sensing system under a bending angle step of 2°.

to the same baseline, suggesting the high repeatability of the sensing system. The minimally detectable bending angle of the system is also tested. As illustrated in Fig. 4(d), the system is capable of distinguishing bending angle of 2°, and the inset shows an enlarged view with distinguished steps.

3. Optoelectronic chip enabled visible light communication

The integration of wireless communication and sensing modules broadens the applications in IoT technology. Normally, the sensing system and communication modules are individually designed and accomplished, leading to high costs and complex configuration. Therefore, an efficient utilization and mutual benefits pursuing between sensing and communication networks is demanded. Herein, apart from the ability of optical sensing, the proposed optoelectronic chip can also be applied for visible light communication (VLC). The schematic diagram of the VLC system is presented in Fig. 5(a). Duplex VLC links are established by using the micro-LED as a transmitter and the on-chip PD as a receiver. The transmission and receiving performance of the chip are test first. Pseudo random binary sequence (PRBS) produced by the signal generator is used to drive the micro-LED. The emitted blue light is focused and directs to the external PD. Similarly, the on-chip PD is irradiated by a modulated 405 nm LD to verify the optical detection. Fig. 5(b) shows the frequency response curve of the micro-LED transmitter under a biased voltage of 3.7 V. The device bandwidths at -3 dB and -10 dB are 12 MHz and 42 MHz, respectively. Normally, micro-LEDs have high modulation bandwidth and
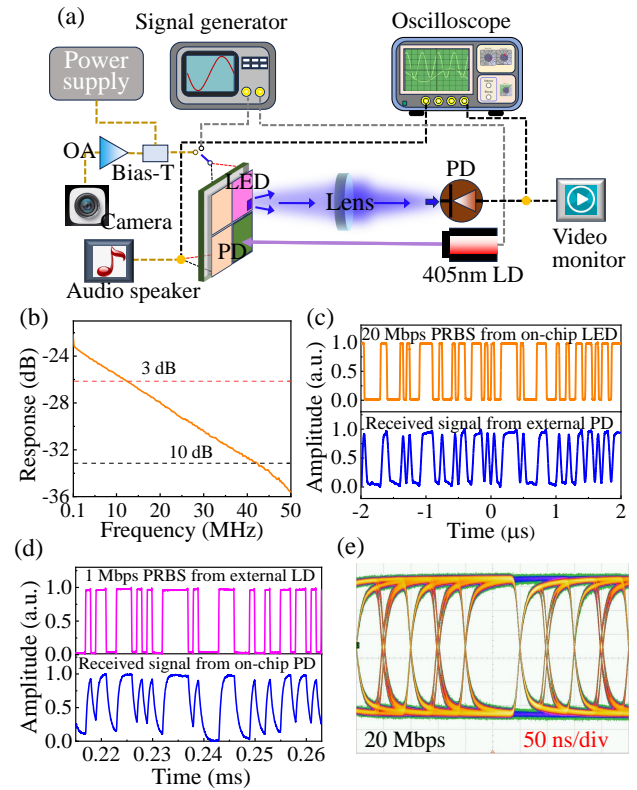

Fig. 5. Experimental results of visible light communication (VLC) when the monolithic optoelectronic chip serves as a transceiver. (a) Experimental setup of the VLC links for audio and video transmission. (b) Bandwidth of the micro-LED. Comparisons between transmitted and received PRBS signals When the system works in the uplink (c) and downlink (d) states, respectively. (e) Eye diagram at 20 Mbps.

are widely employed for high-speed on-chip or free-space communication [28,29,32]. In our results, the frequency bandwidth is limited to tens of megahertz, which is possibly caused by the large resistance-capacitance (RC) time constant associated with our micro-fabrication process. As plotted in the inset in Fig. 2(b), the value of capacitance is around 50 pF before the applied voltage exceeds the turn-on voltage. The resistance of LED is calculated to be approximately 48 Ω from the slope of the linear region of the I-V curve. The big resistance value maybe caused by the poor contact characteristics of metal and semiconductor. The relatively high RC constant limits the frequency bandwidth of the device. Based on the PRBS modulation, the micro-LED is driven at a transmission rate of 20 Mbps, and a commercial PD is used to receive the signal. As recorded in Fig. 5(c), the received signal retains its original waveform profile at 20 Mbps. Fig. 5(d) presents the waveform comparison before and after the on-chip PD reception when the LD is modulated with a data rate of 1 Mbps. The open eye diagram can be clearly seen corresponding to the transmitted rate of 20 Mbps, as illustrated in Fig. 5(e).

Afterwards, real-time audio and video signals transmission are demonstrated with the VLC system. As displayed in Fig. 5(a), the surrounding image is collected by a camera, and the
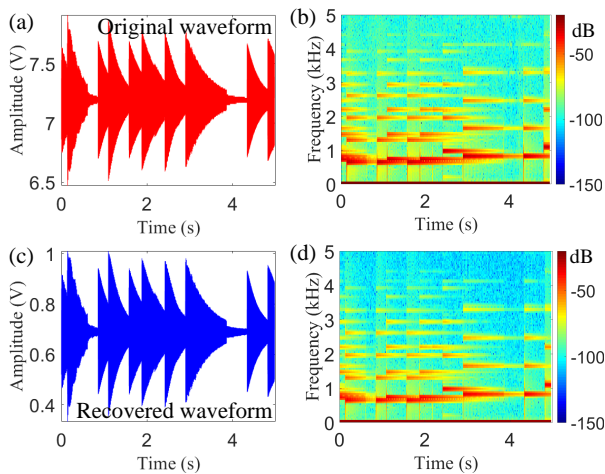
Fig. 6. Comparisons between original and recovered audio signals in the time domain and the frequency domain. The waveform (a) and spectrogram (b) of the original signal. The waveform (c) and spectrogram (d) of the recovered signal.

voltage of the generated data streams is amplified first by an operational amplifier. Then the amplified signal mixed with DC signal through a bias-T is employed to drive the micro-LED. At the receiving part, an external PD converts the optical signal into the electrical signal. The electrical signal is captured via a video capture card, transformed into video signal and displayed on the screen of a terminal monitor in real time (See Visualization 1). For audio signal demonstration, a clip of music "Sky city" is transformed into the data format and loaded in the signal generator to drive an external LD. The driven voltage and amplitude applied to the LD are set to be 3.6 V and 800 mVpp, respectively. The on-chip PD responses to the laser radiation and generates the photocurrent carrying the audio information. The detected audio signal is amplified by a transimpedance amplifier (TIA) and replayed through a speaker (See Visualization 2). The original signal and the recovered audio signal are compared and analyzed in the time domain and frequency domain, respectively. As displayed in Fig. 6(a) and (c), the detected waveform (marked with blue curve) is consistent with the original signal (marked with red curve). The recovered signal nearly retains most of the amplitude information without distortion. Since the audio signal is composed of multiple frequency components, the quality of the received signal depends on the accurate reception of each single frequency. The corresponding spectrograms are analyzed by fast Fourier transform (FFT) to evaluate the signal reconstruction performances. As can be seen in Fig. 6(b) and (d), the frequency distributions of the selected music are below 4 kHz, and mainly in the range from 1 kHz to 2 kHz. In addition, a series of vertical stripes in the spectrogram are clearly observed, which denote the amplitude of the audio signal over the time. In terms of intensity visibility, the recovered signal is weaker than the original signal owing to the reduced amplitude values. But the main frequency components are able to be maintained. As a result, there is no distortion in the sound quality of the recovery signal played through the speaker.

4. Conclusion

In conclusion, we demonstrate a versatile monolithic optoelectronic platform which can be used for fiber sensing as well as visible light communication (VLC). The monolithic integration of the LED and PD efficiently replaces the bulky external light source and detector, which is small in size and low in cost. By configuring this optoelectronic platform, bending angle measurement and audio-video transmission are performed. These proof-of-concept experiments validate the multi-function of the optoelectronic platform, which is expected to build a miniaturized and low-cost integrated optical sensing and communication (IOSAC) system.

References

1. L. Guo, Z. Lu, and L. Yao, "Human-machine interaction sensing technology based on hand gesture recognition: A review", IEEE Trans. Hum.-Mach. Syst. **51**, 300-309 (2021).
2. F. Domingues, N. Alberto, J. Leitao, et al.," Insole optical fiber sensor architecture for remote gait analysis—An e-health solution", IEEE Internet Things J. **6**, 207 (2017).
3. L. L. Li, D. P. Wang, D. Zhang, et al., "Near-Infrared Light Triggered Self-Powered MechanoOptical Communication System using Wearable Photodetector Textile", Adv. Funct. Mater. **31**, 2104782 (2021).
4. D. Lee, J. Yang, J. Sim, et al., " Bending sensor based on controlled micro-cracking regions for application toward wearable electronics and robotics", ACS Appl. Mater. **14**, 31312 (2022).
5. H. Liu, H. Y. Zhao, S. et al., "Adhesion-Free Thin-Film-Like Curvature Sensors Integrated on Flexible and Wearable Electronics for Monitoring Bending of Joints and Various Body Gestures", Adv. Mater. Technol. **4**, 1800327 (2019).
6. S. Zhang, L. Yin, Y. Zhao, et al., "Bending sensor with parallel fiber Michelson interferometers based on Vernier-like effect", Opt. Laser Technol. **120**, 105679 (2019).
7. H. Qu, G. Yan, and M. Skorobogatiy, "Interferometric fiber-optic bending/nano-displacement sensor using plastic dual-core fiber", Opt. Lett. **39**, 4835 (2014).
8. T. Zhou, M. Chen, Z. Hu, et al., "Research on Ultra-Wide Joint Bending Angle Detection Based on Transparent Tubing Structure", IEEE Sens. J. **24**, 1511 (2023).
9. A. Leal-Junior, C. Diaz, C. Marques, et al., "Multiplexing technique for quasi-distributed sensors arrays in polymer optical fiber intensity variation-based sensors", Opt. Laser Technol. **111**, 81 (2019).

10. A. Aitkulov and D. Tosi, "Optical Fiber Sensor Based on Plastic Optical Fiber and Smartphone for Measurement of the Breathing Rate", IEEE Sens. J. **19**, 3283 (2019).

11. L. Lu, Z. Jiang, Y. Hu, et al., "A portable optical fiber SPR temperature sensor based on a smart-phone", Opt. Express **27**, 25420 (2019).

12. C. Chen, H. Ding, Y. Yue, and C. Y. Han, "The self-assembly composite photonic crystal: Toward easy humidity detection by a smartphone", IEEE Photonics Technol. Lett. **32**, 1469 (2020).

13. S. Lo, E. Lin, K. Lee, et al., "A Concave Blazed-Grating-Based Smartphone Spectrometer for Multichannel Sensing", IEEE Sens. J. **19**, 11134 (2019).

14. H. Yu, M. Memon, H. Jia, et al., "Deep-Ultraviolet LEDs Incorporated with SiO2-Based Microcavities Toward High-Speed Ultraviolet Light Communication", Adv. Opt. Mater. **10**, 2201738 (2022).

15. L. Guo, Y. Guo, J. Yang, et al., " 275 nm Deep Ultraviolet AlGaN-Based Micro-LED Arrays for Ultraviolet Communication", IEEE Photonics J. **14**, 8202905 (2022).

16. F. Hu, S. Chen, Y. Zhang, et al., "High-speed visible light communication systems based on Si-substrate LEDs with multiple superlattice interlayers", PhotoniX **2**, 1 (2021).

17. Y. Huang, Z. Guo, X. Wang, et al., "GaN-based high-response frequency and high-optical power matrix micro-LED for visible light communication", IEEE Electron Device Lett. **41**, 1536 (2020).

18. H. Yu, H. Jia, Z. Liu, et al., "Development of highly efficient ultraviolet LEDs on hybrid patterned sapphire substrates", Opt. Lett. **46**, 5356-5359 (2021).

19. F. Wang, L. Jiang, J. Sun, et al., "One-step fabrication method of GaN films for internal quantum efficiency enhancement and their ultrafast mechanism investigation", ACS Appl. Mater. **13**, 7688-7697 (2021).

20. S. Mariana, J. Gulink, G. Hamdana, et al., "Vertical GaN nanowires and nanoscale light-emitting-diode arrays for lighting and sensing applications", ACS Appl. Nano Mater. **2**, 4133 (2019).

21. Y. Dong, D. Son, Q. Dai, et al., "AlGaN/GaN heterostructure pH sensor with multi-sensing segments", Sensor Actuat B-Chem. **260**, 134 (2018).

22. J. Um, D. Jeong, Y. Jung, et al., "Active-Matrix GaN μ-LED Display Using Oxide Thin-Film Transistor Backplane and Flip Chip LED Bonding", Adv. Electron. Mater. **5**, 1800617 (2019).

23. C. Hun, S. Lee, K. Kwon, et al., "A monolithically integrated micro-LED display based on GaN-on-silicon substrate", Appl. Phys. Express **13**, 026501 (2020).

24. S. Zhu, X. Shan, R. Lin, et al., "Characteristics of GaN-on-Si green micro-LED for wide color gamut display and high-speed visible light communication", ACS Photonics **10**, 92-100 (2023).

25. K. Li, W. Fu, Y. Cheung, et al., "Monolithically integrated InGaN/GaN light-emitting diodes, photodetectors, and waveguides on Si substrate", Optica **5**, 564 (2018).

26. L. Wang, X. Li, X. Gao, et al., "Asymmetric optical links using monolithic III-nitride diodes", Opt. Lett. **46**, 376 (2021).

27. Y. Luo, X. An, L. Chen, et al., "Chip-scale optical airflow sensor", Microsyst. Nanoeng. **8**, 4 (2022).

28. H. Yu, S. Xiao, M. Memon, et al., "Dual-Functional Triangular-Shape Micro-Size Light-Emitting and Detecting Diode for On-Chip Optical Communication in the Deep Ultraviolet Band", Laser & Photonics Rev. 2300789 (2024).

29. M. Memon, H. Yu H. Jia, et al., "Quantum Dots Integrated Deep-Ultraviolet Micro-LED Array Toward Solar-Blind and Visible Light Dual-Band Optical Communication", IEEE Electron Device Lett. **44**, 472-475 (2023).

30. P. Liu, Z. Qi, J. Fu, et al., "Unification of irreversibility and energy diagram theory", ACS Omega **8**, 22 (2023).

31. Y. Wang., "Gravitational effect creates the irreversibility", (2023).

32. S. Zhang, R. He, Y. Duo, et al., "Plasmon-enhanced deep ultraviolet Micro-LED arrays for solar-blind communications", Opt. Lett. **48**, 3841-3844 (2023).